International Journal of Modern Physics D
Vol. 19, No. 5 (2010) 607–620

DOI: 10.1142/S0218271810016555

World Scientific
www.worldscientific.com

MONTE CARLO SIMULATIONS OF THE THERMAL COMPTONIZATION PROCESS IN A TWO-COMPONENT ACCRETION FLOW AROUND A BLACK HOLE IN THE PRESENCE OF AN OUTFLOW

HIMADRI GHOSH*, SUDIP K. GARAIN† and
SANDIP K. CHAKRABARTI‡,§

S. N. Bose National Centre for Basic Sciences,
JD-Block, Sector III, Salt Lake, Kolkata 700098, India
**himadri@bose.res.in*
†*sudip@bose.res.in*
‡*chakraba@bose.res.in*

PHILIPPE LAURENT

IRFU, Service d'Astrophysique,
Bat. 709 Orme des Merisiers, CEA Saclay, 91191,
Gif-sur-Yvette Cedex, France
philippe.laurent@cea.fr

Received 13 October 2009
Revised 22 March 2010
Communicated by V. Gurzadyan

A black hole accretion may have both the Keplerian and the sub-Keplerian component. In the so-called Chakrabarti–Titarchuk scenario, the Keplerian component supplies low-energy (soft) photons while the sub-Keplerian component supplies hot electrons which exchange their energy with the soft photons through Comptonization or inverse Comptonization processes. In the sub-Keplerian component, a shock is generally produced due to the centrifugal force. The postshock region is known as the CENtrifugal pressure–supported BOundary Layer (CENBOL). In this paper, we compute the effects of the thermal and the bulk motion Comptonization on the soft photons emitted from a Keplerian disk by the CENBOL, the preshock sub-Keplerian disk and the outflowing jet. We study the emerging spectrum when the converging inflow and the diverging outflow (generated from the CENBOL) are simultaneously present. From the strength of the shock, we calculate the percentage of matter being carried away by the outflow and determine how the emerging spectrum depends on the outflow rate. The preshock sub-Keplerian flow is also found to Comptonize the soft photons significantly. The interplay between the up-scattering and down-scattering effects determines the effective shape of the emerging spectrum. By simulating several cases with various inflow parameters, we conclude that whether the preshock flow, or the postshock CENBOL or the emerging

§Also at: Indian Centre for Space Physics, Chalantika 43, Garia Station Rd., Kolkata 700084, India.

jet is dominant in shaping the emerging spectrum depends strongly on the geometry of the flow and the strength of the shock in the sub-Keplerian flow.

Keywords: Accretion disk; black hole physics; shock waves; radiative processes; Monte Carlo simulations.

1. Introduction

It is well known[3] that the flow velocity is the same as the velocity of light c as the matter enters through the event horizon. However, the sound speed is never so high. Thus, the incoming flow on a black hole is always supersonic and so these solutions are likely to be most relevant in the study of the physical processes around black holes. As the flow begins its journey subsonically very far away, and becomes supersonic on the horizon, the flow is also known as a transonic flow. In the context of the spherical flows, Bondi's solution of accretion and Parker's solution of winds[20] are clear examples of transonic flows. But these flows have only one sonic point. In the presence of angular momentum, the flow may have two saddle type sonic points with a shock in between.[3,9] The solutions with shocks have been extensively studied in both the accretion and the winds even when rotation, heating, cooling, etc. are included.[3,9] The study demonstrates that the accretion and the winds are interrelated — the outflows are generated from the postshock region. Subsequently, in Refs. 5, 10 and 11, the mass outflow rate was computed as a function of the shock strength and other flow parameters. Meanwhile, in the so-called two-component advective flow (TCAF) model of Refs. 8 and 4, the spectral states were shown to depend on the location and strength of the shock. Thus, Ref. 5, for the first time, brought out the relationship between the jets and outflows with the presence or absence of shocks, and therefore with the spectral states of black hole candidates. This paved the way for studying the relative importance between the Compton cloud and the outflow as far as the emerging spectrum is concerned.

In the Chakrabarti–Titarchuk mechanism,[8,7] the computation of the spectral characteristics concentrated on only the accretion, and the effects of the outflow or the base of the jet was not included. In the Monte Carlo simulations of Laurent and Titarchuk,[16] outflows were used only in isolation, but not in conjunction with inflows. In Ref. 12, the Chakrabarti–Titarchuk mechanism for producing various spectral states by varying accretion rates was tested by using Monte Carlo simulations. In the present paper, we extend this work and obtain the outgoing spectrum in the presence of both inflows and outflows. We also include a Keplerian disk inside a sub-Keplerian flow which is the source of soft photons. We show how the spectrum depends on the flow parameters of the inflow, such as the accretion rates of the two components and the shock strength. The postshock region being denser and hotter, it behaves like the so-called "Compton cloud" of the classical model of Sunyaev and Titarchuk.[28] This region is known as the CENtrifugal pressure–supported BOundary Layer (CENBOL). Since the shock location and its strength depend on the inflow parameters, the variation of the size of the Compton cloud, and therefore

the Comptonized component of the spectrum, is a function of the basic parameters of the flow, such as the specific energy, the accretion rate and the specific angular momentum. Since the intensity of soft photons determines the Compton cloud temperature, the result depends on the accretion rate of the Keplerian component also. In our result, we also see the effects of the bulk motion Comptonization,[8] where even a cooler CENBOL produces a harder spectrum. At the same time, the effect of down-scattering due the outflowing electrons is also seen, because of which even a hotter CENBOL causes the disk-jet system to emit less-energetic photons. Thus, the net spectrum is a combination of all these effects.

In the next section, we discuss the geometry of the soft photon source and the Compton cloud in our Monte Carlo simulations. In Sec. 3 we present the variation of the thermodynamic quantities and other vital parameters inside the Keplerian disk and the Compton cloud which are required for the Monte Carlo simulations. In Sec. 4 we describe the simulation procedure, and in Sec. 5 we present the results of our simulations. Finally, in Sec. 6, we make concluding remarks.

2. Geometry of the Electron Cloud and the Soft Photon Source

The problem in hand is very complex and thus we need to simplify the geometry of the inflow–outflow configuration without sacrificing the salient features. In Fig. 1, we present a diagram of our simulation setup. The components of the hot electron clouds, namely the CENBOL, the outflow and the sub-Keplerian flow, intercept the soft photons emerging out of the Keplerian disk and reprocess them via inverse Compton scattering. An injected photon may undergo a single scattering, multiple scatterings or no scattering at all with the hot electrons in between its emergence from the Keplerian disk and its detection by the telescope at a large distance. The photons which enter the black holes are absorbed. The CENBOL, though toroidal in nature, is chosen to be of spherical shape for simplicity. The sub-Keplerian inflow in

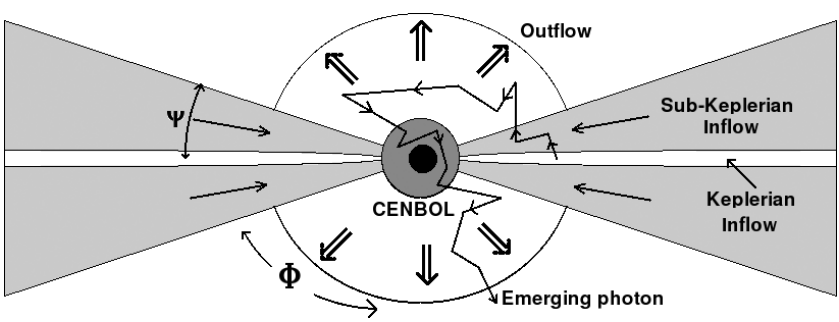

Fig. 1. Diagram of the geometry of our Monte Carlo simulation presented in this paper. The spherical inflowing postshock region (CENBOL) surrounds the black hole and is surrounded by the Keplerian disk on the equatorial plane and a sub-Keplerian halo above and below. A diverging conical outflow is formed from the CENBOL. The typical path of a photon is shown by zigzag paths.

the preshock region is assumed to be of wedge shape with a constant angle, Ψ. The outflow, which emerges from the CENBOL in this picture, is also assumed to be of constant conical angle, Φ. In reality, the inflow and the outflow could have somewhat different shapes, depending on the balance of the force components. However, the final result is not expected to be sensitive to such assumptions.

2.1. *Distribution of temperature and density inside the Compton cloud*

We assume the black hole to be nonrotating and we use the pseudo-Newtonian potential[22] to describe the geometry around a black hole. This potential is $-\frac{1}{2(r-1)}$ (r is in the unit of the Schwarzschild radius $r_g = 2GM/c^2$). Velocities and angular momenta are measured in units of c, the velocity of light, and $r_g c$, respectively. For simplicity, we chose the Bondi accretion solution in pseudo-Newtonian geometry to describe both the accretion and the winds. The equation of motion of the sub-Keplerian matter around the black hole in the steady state is assumed to be given by

$$u\frac{du}{dr} + \frac{1}{\rho}\frac{dP}{dr} + \frac{1}{2(r-1)^2} = 0.$$

Integrating this equation, we get the expression for the conserved specific energy:

$$\epsilon = \frac{u^2}{2} + na^2 - \frac{1}{2(r-1)}. \tag{1}$$

Here P is the thermal pressure and a is the adiabatic sound speed, given by $a = \sqrt{\gamma P/\rho}$, where γ is the adiabatic index and is equal to $\frac{4}{3}$ in our case. The conserved mass flux equation, as obtained from the continuity equation, is given by

$$\dot{m} = \Omega\rho u r^2, \tag{2}$$

where ρ is the density of the matter and Ω is the solid angle subtended by the flow. For an inflowing matter, Ω is given by

$$\Omega_{\rm in} = 4\pi \sin\Psi,$$

where Ψ is the half-angle of the conical inflow. For the outgoing matter, the solid angle is given by

$$\Omega_{\rm out} = 4\pi(1 - \cos\Phi),$$

where Φ is the half-angle of the conical outflow. From Eq. (2), we get

$$\dot{\mu} = a^{2n} u r^2. \tag{3}$$

The quantity $\dot{\mu} = \frac{\dot{m}\gamma^n K^n}{\Omega}$ is the Chakrabarti rate,[2,3,9] which includes the entropy, K being the constant measuring the entropy of the flow, and $n = \frac{1}{\gamma-1}$ is called the polytropic index. Unlike for instance the Bondi rate, which remains constant

throughout the flow, the Chakrabarti rate will change at the shock due to change in entropy (i.e. K). We take the derivative of Eqs. (1) and (3) with respect to r and, eliminating $\frac{da}{dr}$ from both the equations, we get the gradient of the velocity as

$$\frac{du}{dr} = \frac{\dfrac{1}{2(r-1)^2} - \dfrac{2a^2}{r}}{\dfrac{a^2}{u} - u}. \tag{4}$$

From this, we obtain the Bondi accretion and wind solutions in the usual manner.[3] Solving these equations, we obtain u, a and finally the temperature profile of the electron cloud (T_e) using $T_e = \frac{\mu a^2 m_p}{\gamma k_B}$, where $\mu = 0.5$ is the mean molecular weight, m_p the proton mass and k_B the Boltzmann constant. Using Eq. (2), we calculate the mass density ρ, and hence the number density variation of electrons inside the Compton cloud. We ignore the electron–positron pair formation inside the cloud.

The flow is supersonic in the preshock region and subsonic in the postshock (CENBOL) region. We chose the shock location, i.e. the outer boundary of the CENBOL where the preshock Mach number $M = 2$. This location and Mach number depends on the specific energy ϵ.[3] In our simulation, we have chosen $\epsilon = 0.015$ so that we get $R_s = 10$. We simulated a total of six cases. For cases 1(a)–1(c), we chose $\dot{m}_h = 1$, $\dot{m}_d = 0.01$, and for cases 2(a)–2(c) the values are listed in Table 2. The velocity variation of the sub-Keplerian flow is the inflowing Bondi solution (presonic point). The density and the temperature of this flow have been calculated according to the above-mentioned formulas. Inside the CENBOL, the Keplerian and sub-Keplerian components are mixed together. The velocity variation of the matter inside the CENBOL is assumed to be the same as the Bondi accretion flow solution reduced by the compression ratio of the shock. The compression ratio (i.e. the ratio between the postshock and preshock densities) R is used to compute the density and the temperature profile. When the outflow is adiabatic, the ratio of the outflow to the inflow rate[11] is given by

$$R_{\dot{m}} = \frac{\Omega_{\rm out}}{\Omega_{\rm in}} \left(\frac{f_0}{4\gamma}\right)^3 \frac{R}{2} \left[\frac{4}{3}\left(\frac{8(R-1)}{R^2} - 1\right)\right]^{3/2}. \tag{5}$$

Here, we have used $n = 3$ for a relativistic flow. From this, and the velocity variation obtained from the outflow branch of the Bondi solution, we compute the density variation inside the jet. In our simulation, we have used $\Phi = 58^\circ$ and $\Psi = 32^\circ$. This was to ensure that the outflow rate is very high (in this case 97% of the inflow rate) and the disk is not evacuated. Figure 2 shows the variation of the percentage of matter in the outflow for these particular parameters.

2.2. *Keplerian disk*

The soft photons are produced from a Keplerian disk whose inner edge coincides with the CENBOL surface, while the outer edge is located at $500r_g$. The source of soft photons has a multicolor blackbody spectrum coming from a standard[25]

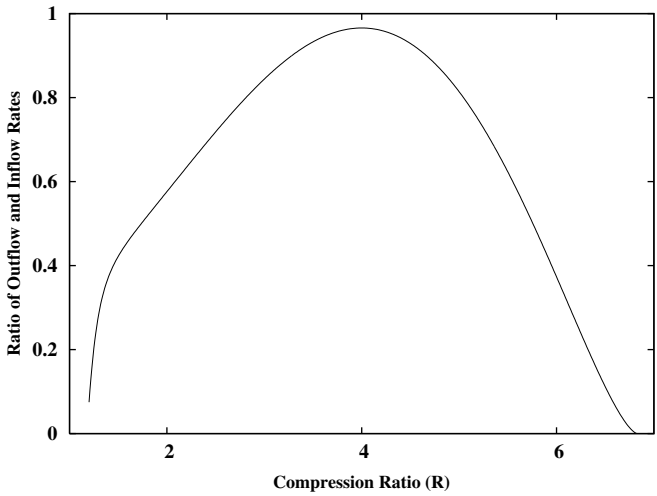

Fig. 2. Ratio of the outflow and inflow rates as a function of the compression ratio R of the inflow when the outflow is adiabatic. In our simulations, we have used the jet angle as 58°.

disk. We assume the disk to be optically thick, and the opacity due to free–free absorption is more important than the opacity due to scattering. The emission is blackbody-type, with the local surface temperature[25]

$$T(r) \approx 5 \times 10^7 (M_{\rm bh})^{-1/2} (\dot{M}_{d17})^{1/4} (2r)^{-3/4} \left(1 - \sqrt{\frac{3}{r}}\right)^{1/4} K. \tag{6}$$

The photon flux emitted from the disk surface is obtained by integrating over all frequencies (ν) and is given by

$$n_\gamma(r) = \left[16\pi \left(\frac{k_b}{hc}\right)^3 \times 1.202057\right] (T(r))^3 . \tag{7}$$

The disk between radius r and $r + \delta r$ injects a $dN(r)$ amount of soft photons:

$$dN(r) = 4\pi r \delta r H(r) n_\gamma(r), \tag{8}$$

where $H(r)$ is the half-height of the disk, given by

$$H(r) = 10^5 \dot{M}_{d17} \left(1 - \sqrt{\frac{3}{r}}\right) \text{cm}. \tag{9}$$

The soft photons are generated isotropically between the inner and the outer edge of the Keplerian disk but their positions are randomized using the above distribution function [Eq. (8)] of the blackbody temperature $T(r)$. All the results of the simulations presented here have used the number of injected photons as 6.4×10^8. In the above equations, the mass of the black hole $M_{\rm bh}$ is measured in units of the mass of the Sun ($M_\odot$), and the disk accretion rate $\dot{M}_{d17}$ is in units of 10^{17} gm/s. We chose $M_{\rm bh} = 10$ and $\delta r = 0.5 r_g$.

2.3. *Simulation procedure*

In a given simulation, we assume a given Keplerian rate and a given sub-Keplerian halo rate. The specific energy of the halo provides hydrodynamic properties (such as the number density of the electrons and the velocity variation) and the thermal properties of matter. Since we chose the Paczynski–Wiita potential,[23] the radial velocity is not exactly unity at $r = 1$, the horizon, but it becomes unity just outside. In order not to overestimate the effects of bulk motion Comptonization, which is due to the momentum transfer of the moving electrons to the horizon, we shift the horizon just outsize $r = 1$, where the velocity is unity. The shock location of the CENBOL is chosen where the Mach number $M = 2$ for simplicity and the compression ratio at the shock is assumed to be a free parameter. These simplifying assumptions are not expected to affect our conclusions. Photons are generated from the Keplerian disk according to the prescription in Ref. 25 as mentioned before, and are injected into the sub-Keplerian halo, the CENBOL and the outflowing jet.

In a simulation, we randomly generated a soft photon out of the Keplerian disk. The energy of the soft photon at the radiation temperature $T(r)$ is calculated using Planck's distribution formula, where the number density of the photons $[\bar{N}_\gamma(E)]$ having energy E is expressed by

$$\bar{N}_\gamma(E) = \frac{1}{2\zeta(3)} b^3 E^2 (e^{bE} - 1)^{-1}, \tag{10}$$

where $b = 1/kT(r)$ and $\zeta(3) = \sum_1^\infty l^{-3} = 1.202$; $\zeta(3)$ is the usual Riemann zeta function $\zeta(m)$ for $m = 3$.

Using another set of random numbers we obtained the direction of the injected photons, and with yet another random number we obtained a target optical depth τ_c at which the scattering takes place. The photon was followed within the CENBOL till the optical depth (τ) reached τ_c. The increase in the optical depth ($d\tau$) during its traveling of a path of length dl inside the electron cloud is given by $d\tau = \rho_n \sigma dl$, where ρ_n is the electron number density.

The total scattering cross section σ is given by the Klein–Nishina formula:

$$\sigma = \frac{2\pi r_e^2}{x}\left[\left(1 - \frac{4}{x} - \frac{8}{x^2}\right)\ln(1+x) + \frac{1}{2} + \frac{8}{x} - \frac{1}{2\,(1+x)^2}\right], \tag{11}$$

where x is given by

$$x = \frac{2E}{mc^2}\gamma\left(1 - \mu\frac{v}{c}\right), \tag{12}$$

$r_e = e^2/mc^2$ is the classical electron radius and m is the mass of the electron.

We have assumed here that a photon of energy E and momentum $\frac{E}{c}\widehat{\Omega}$ is scattered by an electron of energy γmc^2 and momentum $\overrightarrow{\mathbf{p}} = \gamma m \overrightarrow{\mathbf{v}}$, with $\gamma = (1 - \frac{v^2}{c^2})^{-1/2}$ and $\mu = \widehat{\Omega} \cdot \widehat{\mathbf{v}}$. At this point a scattering is allowed to take place. The photon selects an electron and the energy exchange is computed through the Compton or inverse Compton scattering formula. The electrons are assumed to

obey relativistic Maxwell distribution inside the CENBOL. The number $dN(p)$ of Maxwellian electrons having momentum between $\mathbf{p}$ and $\mathbf{p} + d\mathbf{p}$ is expressed by

$$dN(\mathbf{p}) = \exp\left[\frac{-(p^2c^2 + m^2c^4)^{1/2}}{kT_e}\right] d\mathbf{p}. \tag{13}$$

Generally, the same procedure as in Ref. 12 was used, except that we are now focusing also on those photons which were scattered at least once by the outflow. In particular, we are choosing the cases where the jet could play a major role in shaping the spectrum. This was done by using the opening angle of the jet close to the maximum, as discussed earlier.

3. Results and Discussions

In Figs. 3(a)–3(c) we present the velocity, electron number density and temperature variations as functions of the radial distance from the black hole for specific energy $\epsilon = 0.015$. We chose $\dot{m}_d = 0.01$ and $\dot{m}_h = 1$. Three cases were run by varying the compression ratio R. They are shown in column 2 of Table 1. The corresponding percentage of matter going in the outflow is also given in the column. In the left panel, the bulk velocity variation is shown. The solid, dotted and dashed curves are the same for $R = 2$ [case 1(a)], 4 [case 1(b)] and 6 [case 1(c)], respectively. The same line style is used in other panels. The velocity variation within the jet does not change with R, but the density (in the unit of cm^{-3}) does (middle panel). The double-dot–dashed line gives the velocity variation of the matter within the jet for all the above cases. The arrows show the directions of the bulk velocity

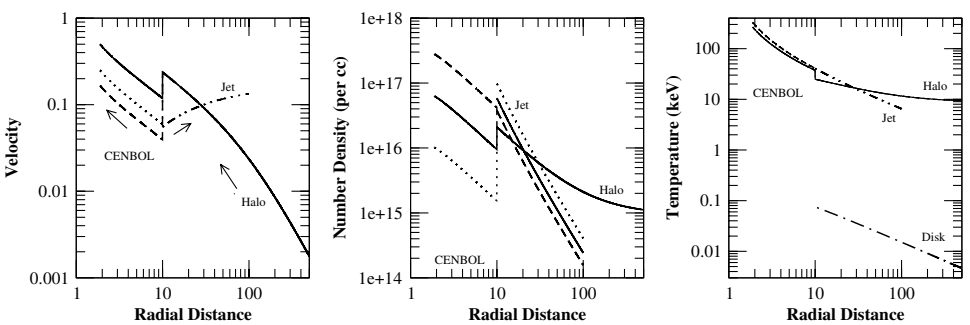

Fig. 3. (a)–(c) Velocity (left), density (middle) and temperature (right) profiles of cases 1(a)–1(c) as described in Table 1 are shown with solid ($R = 2$), dotted ($R = 4$) and dashed ($R = 6$) curves. $\dot{m}_d = 0.01$ and $\dot{m}_h = 1$ were used.

Table 1.

Case	R, P_m	$N_{\rm int}$	$N_{\rm cs}$	$N_{\rm CENBOL}$	$N_{\rm jet}$	$N_{\rm subkep}$	$N_{\rm cap}$	p	α
1(a)	2, 58	2.7E + 08	4.03E + 08	1.35E + 07	7.48E + 07	8.39E + 08	3.35E + 05	63	0.43
1(b)	4, 97	2.7E + 08	4.14E + 08	2.39E + 06	1.28E + 08	8.58E + 08	3.27E + 05	65	1.05
1(c)	6, 37	2.7E + 08	3.98E + 08	5.35E + 07	4.75E + 07	8.26E + 08	3.07E + 05	62	−0.4

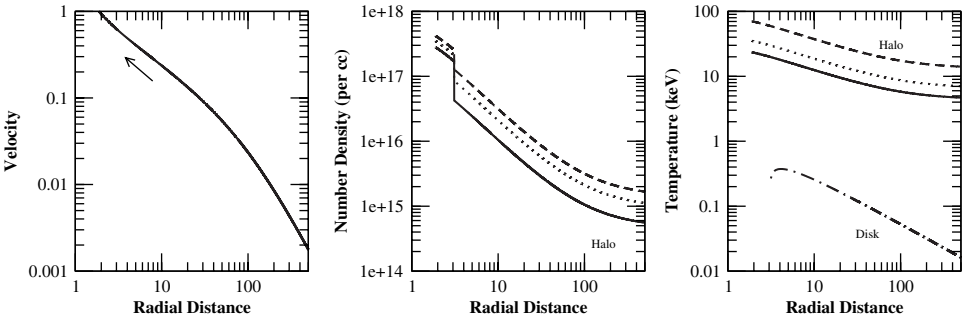

Fig. 4. (a)–(c) Velocity (left), density (middle) and temperature (right) profiles of cases 2(a)–2(c) as described in Table 2 are shown with solid ($\dot{m}_h = 0.5$), dotted (1) and dashed (1.5) curves. $\dot{m}_d = 1.5$ was used throughout. Velocities are the same for all the disk accretion rates.

(radial direction in accretion; vertical direction in jets). The last panel gives the temperature (in keV) of the electron cloud in the CENBOL, jet, sub-Keplerian and Keplerian disk. The big-dash–dotted line gives the temperature profile inside the Keplerian disk.

In Figs. 4(a)–4(c), we show the velocity (left), number density of electrons (middle) and temperature (right) profiles of cases 2(a)–2(c), as described in Table 2. Here we have fixed $\dot{m}_d = 1.5$, and $\dot{m}_h$ is varied: $\dot{m}_h = 0.5$ (solid), 1 (dotted) and 1.5 (dashed). No jet is present in this case ($R = 1$). To study the effects of bulk motion Comptonization, the temperature of the electron cloud has been kept low for these cases. The temperature profile in the different cases has been chosen according to Fig. 3(b) of Ref. 8. The temperature profile of the Keplerian disk for the above cases is marked "Disk".

In Table 1, we summarize the details of all the cases, the results of which are depicted in Figs. 3(a)–3(c). In column 1, various cases are marked. In column 2, the compression ratio (R) and percentage P_m of the total matter that is going out as outflow (see Fig. 2) are listed. In column 3, we show the total number of photons (out of the total injection of 6.4×10^8) intercepted by the CENBOL and jet ($N_{\rm int}$) combined. Column 4 gives the number of photons ($N_{\rm cs}$) that have suffered Compton scattering inside the flow. Columns 5–7 show the number of scatterings which took place in the CENBOL ($N_{\rm CENBOL}$), in the jet ($N_{\rm jet}$) and in the preshock sub-Keplerian halo ($N_{\rm sub\text{-}Kep}$), respectively. A comparison of them will give the relative importance of these three subcomponents of the sub-Keplerian disk. The number of photons captured ($N_{\rm cap}$) by the black hole is given in column 8.

Table 2.

Case	$\dot{m}_h$, $\dot{m}_d$	$N_{\rm int}$	$N_{\rm cs}$	$N_{\rm ms}$	$N_{\rm sub\text{-}Kep}$	$N_{\rm cap}$	p	α_1, α_2
2(a)	0.5, 1.5	1.08E+06	2.13E+08	7.41E+05	3.13E+08	1.66E+05	33.34	−0.09, 0.4
2(b)	1.0, 1.5	1.22E+06	3.37E+08	1.01E+06	6.82E+08	2.03E+05	52.72	−0.13, 0.75
2(c)	1.5, 1.5	1.34E+06	4.15E+08	1.26E+06	1.11E+09	2.29E+05	64.87	−0.13, 1.3

In column 9, we give the percentage p of the total injected photons that have suffered scattering through the CENBOL and the jet. In column 10, we present the energy spectral index α $[I(E) \sim E^{-\alpha}]$ obtained from our simulations.

In Table 2, we summarize the results of simulations where we have varied $\dot{m}_d$, for a fixed value of $\dot{m}_h$. In all of these cases no jet comes out of the CENBOL (i.e. $R = 1$). In the last column, we list two spectral slopes, α_1 (from 10 to 100 keV) and α_2 (due to the bulk motion Comptonization). Here, $N_{\rm ms}$ represents the photons that have suffered scattering between $r_g = 3$ and the horizon of the black hole.

In Fig. 5, we show the variation of the spectrum in the three simulations presented in Figs. 3(a)–3(c). The dashed, dash–dotted and double-dot–dashed lines are for $R = 2$ [case 1(a)], $R = 4$ [case 1(b)] and $R = 6$ [case 1(c)], respectively. The solid curve gives the spectrum of the injected photons. Since the density, velocity and temperature profiles of the preshock sub-Keplerian region and the Keplerian flow are the same in all these cases, we find that the difference in the spectrum is mainly due to the CENBOL and the jet. In the case of the strongest shock (compression ratio $R = 6$), only 37% of the total injected matter goes out as the jet. At the same time, due to the shock, the density of the postshock region increases by a factor of 6. Out of the three cases, the effective density of the matter inside the CENBOL, is the highest, and that inside the jet is the lowest in this case. Again, due to the shock, the temperature increases inside the CENBOL and hence the spectrum is the hardest. Similar effects are seen for moderate shock ($R = 4$) and, to a lesser extent, low strength shock ($R = 2$) also. When $R = 4$, the density of

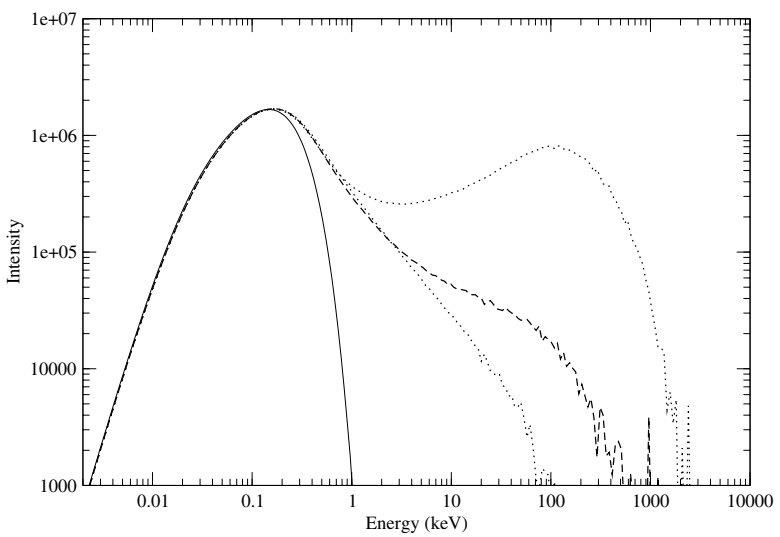

Fig. 5. Variation of the emerging spectrum for different compression ratios. The solid curve is the injected spectrum from the Keplerian disk. The dashed, dash–dotted and double-dot–dashed lines are for $R = 2$ [case 1(a)], $R = 4$ [case 1(b)] and $R = 6$ [case 1(c)], respectively. The disk and halo accretion rates used for these cases are $\dot{m}_d = 0.01$ and $\dot{m}_h = 1$. See text for details.

the postshock region increases by the factor of 4 while almost 97% of the total injected matter (Fig. 2) goes out as the jet, reducing the matter density of the CENBOL significantly. From Table 1 we find that $N_{\rm CENBOL}$ is the lowest and $N_{\rm jet}$ the highest in this case [case 1(b)]. This decreases the up-scattering and increases the down-scattering of the photons. This explains why the spectrum is the softest in this case. In the case of low strength shock ($R = 2$), 57% of the inflowing matter goes out as the jet, but due to the shock the density increases by a factor of 2 in the postshock region. This makes the density similar to a nonshock case as far as the density is concerned, but with a little higher temperature of the CENBOL due to the shock. So the spectrum with the shock would be harder than when the shock is not present. The disk and the halo accretion rates used for these cases are $\dot{m}_d = 0.01$ and $\dot{m}_h = 1$.

In Fig. 6, we show the components of the emerging spectrum for all the three cases presented in Fig. 5. The solid curve indicates the intensity of all the photons which suffered at least one scattering. The dashed curve corresponds to the photons emerging from the CENBOL region, and the dash–dotted curve is for the photons coming out of the jet region. We find that the spectrum from the jet region is softer than the spectrum from the CENBOL. As $N_{\rm jet}$ increases and $N_{\rm CENBOL}$ decreases, the spectrum from the jet becomes softer, for two reasons. First, the temperature of the jet is less than that of the CENBOL, so the photons get a smaller amount of energy from thermal Comptonization, making the spectrum softer. Second, the photons are down-scattered by the outflowing jet, which eventually makes the spectrum softer. We note that a larger number of photons are present in the spectrum from the jet than in the spectrum from the CENBOL, which shows that the photons have actually been down-scattered. The effect of down-scattering is larger when $R = 4$. For $R = 2$ also, there is a significant amount of down-scattered photons. But this number is very small for the case $R = 6$, as $N_{\rm CENBOL}$ is much larger than $N_{\rm jet}$ and so most of the photons get up-scattered. The difference between

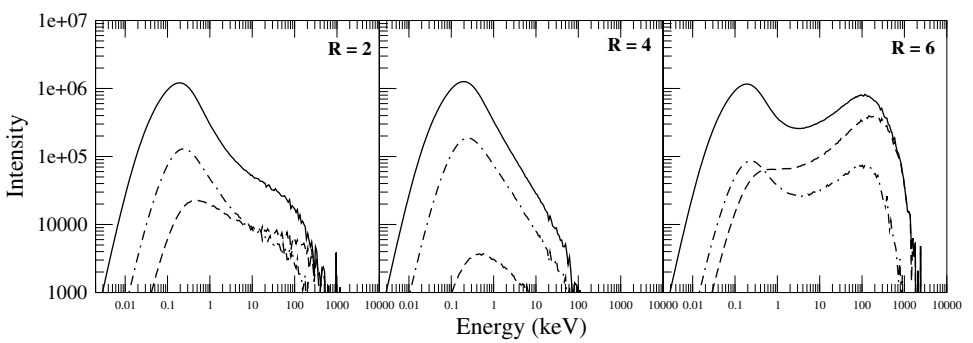

Fig. 6. (a)–(c) Variation of the components of the emerging spectrum with the shock strength (R). The dashed curves correspond to the photons emerging from the CENBOL region and the dash–dotted curves are for the photons coming out of the jet region. The solid curve is the spectrum for all the photons that have suffered scatterings. See text for details.

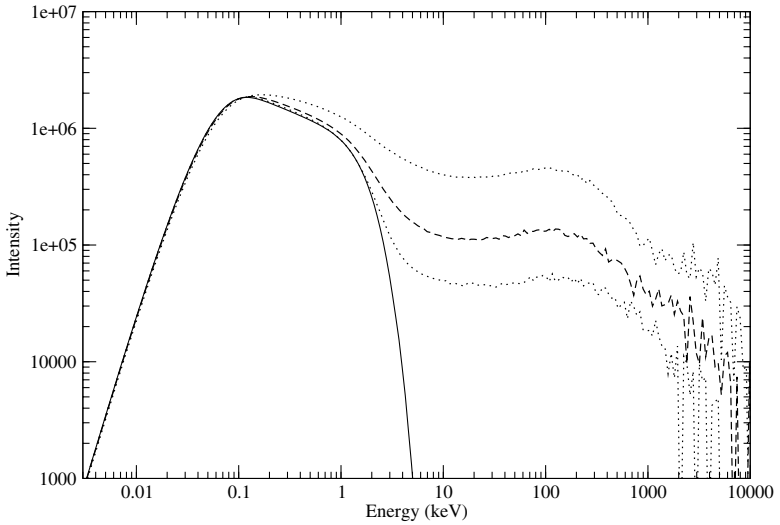

Fig. 7. Bulk motion Comptonization spectrum: solid (injected), dotted ($\dot{M}_h = 0.5$), dashed ($\dot{M}_h = 1$), dash–dotted ($\dot{M}_h = 1.5$). $\dot{M}_d = 1.5$ for all the cases. The Keplerian disk extends up to $3.1r_g$. Table 2 summarizes the parameters used and the simulation results for these cases.

the total (solid) and the sum of the other two regions gives an idea of the contribution from the sub-Keplerian halo located in the preshock region. In our choice of geometry (half-angles of the disk and the jet), the contribution of the preshock flow is significant. In general, it could be much less. This is especially true when the CENBOL is farther out.

In Fig. 7, we show the emerging spectra due to the bulk motion Comptonization when the halo rate is varied. The solid curve is the injected spectrum (modified blackbody). The dotted, dashed and dash–dotted curves are for $\dot{m}_h = 0.5,\ 1,\ 1.5$, respectively. $\dot{m}_d = 1.5$ for all the cases. The Keplerian disk extends up to $3r_g$. Table 2 summarizes the parameter used and the results of the simulation. As the halo rate increases, the density of the CENBOL also increases, causing a larger number of scatterings. From Fig. 4(a), we notice that the bulk velocity variation of the electron cloud is the same for all the four cases. Hence, in the case where the density is maximum, the photons get energized to a very high value due to repeated scatterings with that high velocity cold matter. As a result, there is a hump in the spectrum around 100 keV energy for all the cases. We find the signature of two power law regions in the higher-energy part of the spectrum. The spectral indices are given in Table 2. It is to be noted that α_2 increases with $\dot{m}_h$ and becomes softer for high $\dot{m}_h$. Our geometry here at the inner edge is conical, which is more realistic, unlike a sphere (perhaps nonphysically so) in Ref. 15. This may be the reason why our slope is not the same as in that reference, where $\alpha_2 = 1.9$. In Fig. 8, we present the components of the emerging spectra. As in Fig. 6, solid curves show the spectra of all the photons that have suffered scattering. The dashed and dash–dotted curves

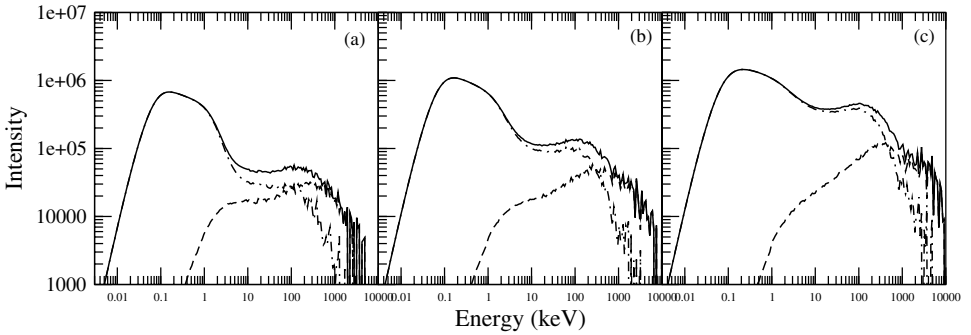

Fig. 8. Components of the emerging spectrum for cases 2(a)–2(c). The solid curves show the spectra of all the photons that have suffered scattering. The dashed and dash–dotted curves show the spectra of photons which are emitted from inside and outside of the marginally stable orbit ($3r_g$), respectively. The photons from inside the marginally stable radius are Comptonized by the bulk motion of the infalling matter. Here the jet is absent.

show the spectra of photons emitted from inside and outside of the marginally stable orbit ($3r_g$), respectively. The photons from inside the marginally stable radius are Comptonized by the bulk motion of the converging infalling matter and produce the power law tail, whose spectral index is given by α_2 (Table 2).

4. Concluding Remarks

In this paper, we have extended the results of our previous work on Monte Carlo simulations.[12] We included the outflow in conjunction with the inflow. The outflow rate was self-consistently computed from the inflow rate using well-known considerations present in the literature (Ref. 11 and references therein). We computed the effects of the thermal Comptonization and bulk motion Comptonization on the soft photons emitted from a Keplerian disk around a black hole by the postshock region of a sub-Keplerian flow which surrounds the Keplerian disk. A shock in the inflow increases the CENBOL temperature, increases the electron number density and reduces the bulk velocity. Thermal Comptonization and bulk motion Comptonization inside the CENBOL increase the photon energy. However, the CENBOL also generates the outflow of matter, which down-scatters the photons to lower energy. We showed that thermal Comptonization and bulk motion Comptonization were possible by both the accretion and the outflows. While the converging flow up-scatters the radiation, the outflow down-scatter it. However, the net effect is not simple. The outflow parameters are strongly coupled to the inflow parameters and thus, for a given inflow and outflow geometry, the strength of the shock can also determine whether the net scattering by the jets would be significant or not. Sometimes the spectrum may become very complex, with two power law indices — one from the thermal and the other from the bulk motion Comptonization. Since the volume of the jet may be larger than that of the CENBOL, sometimes the number of scatterings suffered by softer photons from the electrons in the jet may

be high. However, whether the CENBOL or the jet emerging from it will dominate in shaping the spectrum depends strongly on the geometry of the flow and the strength of the shock. We also found that the halo can Comptonize and harden the spectrum even without the CENBOL. In future, we shall look for signatures of such effects in the observed spectrum, which will enable us to self-consistently derive the accretion and jet parameters.

Acknowledgment

The work of H. Ghosh is supported by a RESPOND project.

References

1. H. Bondi, *Mon. Not. R. Astron. Soc.* **112** (1952) 195.
2. S. K. Chakrabarti, *Astrophys. J.* **347** (1989) 365.
3. S. K. Chakrabarti, *Theory of Transonic Astrophysical Flows* (World Scientific, Singapore, 1990).
4. S. K. Chakrabarti, *Astrophys. J.* **484** (1997) 313.
5. S. K. Chakrabarti, *Astron. Astrophys.* **351** (1999) 185.
6. S. K. Chakrabarti, L. Jin and W. D. Arnett, *Astrophys. J.* **313** (1987) 674.
7. S. K. Chakrabarti and S. Mandal, *Astrophys. J.* **642** (2006) L49.
8. S. K. Chakrabarti and L. G. Titarchuk, *Astrophys. J.* **455** (1995) 623.
9. S. K. Chakrabarti, L. G. Titarchuk, D. Kazanas and K. Ebisawa, *Astron. Astrophys. Suppl. Ser.* **120** (1996) 163.
10. T. K. Das and S. K. Chakrabarti, *Class. Quantum Grav.* **16** (1999) 3879.
11. S. Das, I. Chattopadhyay, A. Nandi and S. K. Chakrabarti, *Astron. Astrophys.* **379** (2001) 683.
12. H. Ghosh, S. K. Chakrabarti and P. Laurent, *Int. J. Mod. Phys.* **18** (2009) 1693.
13. J. M. Hua and L. G. Titarchuk, *Astrophys. J.* **469** (1996) 280.
14. P. Laurent and L. G. Titarchuk, *Astrophys. J.* **511** (1999) 289.
15. P. Laurent and L. G. Titarchuk, *Astrophys. J.* **562** (2001) 67.
16. P. Laurent and L. Titarchuk, *Astrophys. J.* **656** (2007) 1056.
17. D. Molteni, G. Lanzafame and S. K. Chakrabarti, *Astrophys. J.* **425** (1994) 161.
18. D. Molteni, D. Ryu and S. K. Chakrabarti, *Astrophys. J.* **470** (1996) 460.
19. I. Novikov and K. S. Thorne, in *Black Holes*, eds. C. DeWitt and B. DeWitt (Gordon and Breach, New York, 1973), p. 343.
20. E. N. Parker, *Astrophys. J.* **129** (1959) 217.
21. L. A. Pozdnyakov, I. M. Sobol and R. A. Sunyaev, *Astrophys. Space Sci. Rev.* **2** (1983) 189.
22. B. Paczyński and P. J. Wiita, *Astron. Astrophys.* **88** (1980) 23.
23. M. J. Rees, M. C. Begelman, R. D. Blandford and E. S. Phinney, *Nature* **295** (1982) 17.
24. G. Rybicki and A. P. Lightman, *Radiative Processes in Astrophysics* (Wiley Interscience, New York, 1979).
25. N. I. Shakura and R. A. Sunyaev, *Astron. Astrophys.* **24** (1973) 337.
26. S. L. Shapiro and S. A. Teukolsky, *Black Holes, White Dwarfs and Neutron Stars: The Physics of Compact Objects* (John Wiley and Sons, New York, 1983).
27. R. A. Sunyaev and L. G. Titarchuk, *Astron. Astrophys.* **143** (1985) 374.
28. R. A. Sunyaev and L. G. Titarchuk, *Astron. Astrophys.* **86** (1980) 121.
29. L. G. Titarchuk, *Astrophys. J.* **434** (1994) 570.